RESEARCH ARTICLE

The pteropod species *Heliconoides inflatus* as an archive of late Pleistocene to Holocene environmental conditions on the Northwest Shelf of Australia

Maximilian Hallenberger[1]*, Lars Reuning[2], Hideko Takayanagi[3], Yasufumi Iryu[3], Nina Keul[2],
Takeshige Ishiwa[4] and Yusuke Yokoyama[5]

Abstract

There is growing interest in the use of pteropods as potential archives of past changes in ocean chemistry. However, pteropods have rarely been used in studies of millennial-scale sedimentary records, especially in shallow-marine environments. This study obtained core data for the last 16 kyr from the Northwest Shelf of Australia (NWS). Changes in the carbonate saturation state were assessed based on the carbon isotope ratios (δ^{13}C) of shells and the *Limacina* dissolution index (LDX) measured on the planktonic pteropod species *Heliconoides inflatus*. In addition, the calcification depth of the pteropods was estimated based on oxygen isotope values (δ^{18}O) of pteropod shells and seawater. Our findings indicate that *H. inflatus* calcifies at a depth of 95–140 m. This confirms that *H. inflatus* records a shallow-marine signal on the NWS. The δ^{13}C values of the pteropods record a notable decrease in carbonate ion concentrations after 8.5 ka. This decrease is associated with the post-glacial onset of humid conditions on the NWS. The studied pteropod shells are pristine throughout the 16 kyr section and have low LDX values. Therefore, the LDX proxy appears to lack the sensitivity to be applicable in this highly supersaturated, shallow-marine environment. Until this study, proxies derived from *H. inflatus* have been exclusively utilized in open-marine settings. Our results indicate that the δ^{13}C values of *H. inflatus* also represent a useful proxy for carbonate ion concentrations in shallow-marine environments.

Keywords: Carbonate ion concentration, Pelagic gastropod, Indo-Pacific Ocean, *Limacina* dissolution index, Carbon and oxygen isotopes, Sedimentary core record

1 Introduction

Ocean water chemistry parameters, such as carbonate ion concentrations and the saturation states of carbonate minerals, have an important role in the production of carbonates in low-latitude shallow-marine environments. This includes the (inorganic) precipitation of aragonite mud (Shinn et al. 1989; Robbins and Blackwelder 1992; Purkis et al. 2017) and the formation of non-skeletal grains (Li et al. 2015; Trower et al. 2017; Harris et al. 2019), both of which are dependent on elevated carbonate saturation states. In addition, carbonate saturation is a controlling factor on the calcification rates and fitness of calcifying organisms (Manno et al. 2017).

On the Northwest Shelf of Australia (NWS), cyclical changes in carbonate sedimentation have been linked to climate-related changes in carbonate saturation states (Hallenberger et al. 2019, 2021). Low fluvial runoff (Ishiwa et al. 2019; Courtillat et al. 2020) and high rates of evaporation have been proposed to have resulted in

---

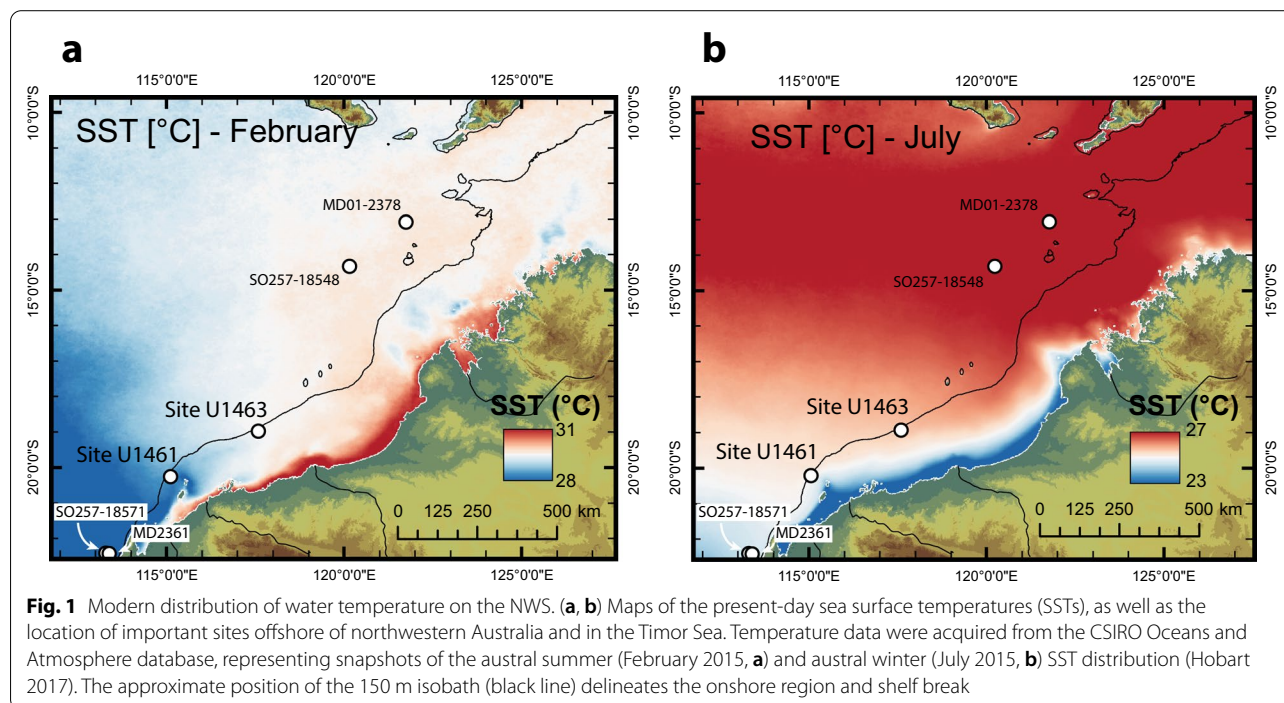*Correspondence: maximilian.hallenberger@emr.rwth-aachen.de
[1] Energy and Mineral Resources Group (EMR), Geological Institute, RWTH Aachen University, Wuellnerstrasse 2, 52062 Aachen, Germany
Full list of author information is available at the end of the article

elevated ocean water carbonate saturation during comparatively dry glacial stages (Hallenberger et al. 2019). This led to the formation of extensive platform systems consisting of ooids (Gallagher et al. 2014, 2018; Hallenberger et al. 2021), as well as the deposition of large volumes of aragonite needle mud (Dix et al. 2005; Hallenberger et al. 2021). In comparison, the interglacial stages were defined by a more humid climate, and the deposition was dominated by skeletal calcite grains (Hallenberger et al. 2019, 2021). However, glacial to interglacial proxy records for changes in ocean water chemistry on the NWS, thereby impeding the significance of previous interpretations linking climate and cyclical sedimentation. In this paper, we address this issue by utilizing proxy data derived from the aragonitic shells of the cosmopolitan euthecosomatous pteropod (i.e., pelagic gastropod) *Heliconoides inflatus* (d'Orbigny 1843), also known as *Limacina inflata* (Janssen 2012). Aragonitic pteropods are particularly useful in predicting the carbonate saturation state of shallow ocean waters due to their sensitivity to changes in ocean acidification and abundance in shallow water depths (Bé and Gilmer 1977; Bednaršek et al. 2012; Keul et al. 2017). In addition, *H. inflatus* is characterized by a 1-yr life cycle and diel migration (Wormuth, 1981; Almogi-Labin et al., 1988). Therefore, carbonate ion concentrations derived from the shells of *H. inflatus* represent an integrated proxy record, making this species a promising target for the reconstruction of past ocean water conditions on shallow shelf areas

(Juranek et al. 2003; Keul et al. 2017; Oakes et al. 2021). More commonly, carbonate ion concentrations have been determined based on different proxies derived from foraminiferal shells, including boron-to-calcium ratios (Yu and Elderfield 2007; Yu et al. 2010), uranium-to-calcium ratios (Raitzsch et al. 2011; Keul et al. 2013), and boron isotopic compositions (δ^{11}B values; Yu and Elderfield 2007). While these proxies have been proven to yield robust constraints on carbonate ion concentrations (Yu et al. 2010), these proxies are of limited use in a shallow-marine setting, where temporal variations in oceanic and climatic conditions combined with the ≤ 1 yr lifespan can result in a strong seasonal bias.

To constrain the changes in ocean water chemistry over the last deglacial transition, we studied sediment core records covering the last 16 kyr from the International Ocean Discovery Program (IODP) Sites U1461 and U1463 (Fig. 1). Changes in carbonate ion concentrations were determined based on the stable carbon isotope ratios (δ^{13}C values) of *H. inflatus* shells (Keul et al. 2017). The *H. inflatus* shells were further screened for their preservation state (*Limacina* dissolution index [LDX] values), which is a parameter that is directly linked to the aragonite saturation state of the ambient seawater (Gerhardt and Henrich 2001; Wall-Palmer et al. 2013, 2014).

The interpretation of *H. inflatus*-based proxy data is complicated by the limited knowledge of its calcification depth. *Heliconoides inflatus* inhabits a large range of depths from the sea surface down to 1000 m (Wormuth

Fig. 1 Modern distribution of water temperature on the NWS. (**a**, **b**) Maps of the present-day sea surface temperatures (SSTs), as well as the location of important sites offshore of northwestern Australia and in the Timor Sea. Temperature data were acquired from the CSIRO Oceans and Atmosphere database, representing snapshots of the austral summer (February 2015, **a**) and austral winter (July 2015, **b**) SST distribution (Hobart 2017). The approximate position of the 150 m isobath (black line) delineates the onshore region and shelf break

1981; Juranek et al. 2003; Bednaršek et al. 2012; Keul et al. 2017). *Heliconoides inflatus* undergoes diel vertical migration, with the highest population densities at < 75 m depth during the night and at > 200 m depth during the day (Wormuth 1981). The main driver for this day–night cycle, which can reach a vertical migration depth range of > 250 m (Chen and Bé 1964; Wormuth 1981), is food availability and the presence of predatory species (Wormuth 1981; Almogi-Labin et al. 1988; Juranek et al. 2003; Oakes and Sessa 2020). *Heliconoides inflatus* also displays ontogenetical migration patterns, with juveniles staying near the sea surface, and adults found in deeper water (Almogi-Labin et al. 1988).

To determine the depth range recorded by the pteropods, oxygen isotope data for *H. inflatus* were compared with the present-day conditions on the NWS, as well as more established proxy data, including for benthic (*Uvigerina* spp.) and planktonic (*Globorotalia menardii*) foraminifera.

2 Modern oceanographic setting

The climate and oceanography of the NWS are influenced by strong seasonal changes between the austral summer (December–March) and austral winter (June–August) (Sudmeyer 2016). In general, the NWS is characterized by subtropical arid conditions, with an annual rainfall of ~ 320 mm (Sudmeyer 2016). Most (~ 60%) of the precipitation in northwestern Australia occurs seasonally during the Australian Summer Monsoon (Lough 1998; Hesse et al. 2004). In addition, strong cyclones occur during austral summer months, resulting in torrential rainfall, flash floods, and rapid discharge of fluvial sediments (Fandry and Steedman 1994; Condie et al. 2003). Surface air temperatures are highest during the austral summer months, with average values > 30 °C. In comparison, air temperatures drop to an average of 20 °C during the austral winter (Sudmeyer 2016).

Water temperatures on the NWS vary significantly depending on the season, water depth, and distance from shore (Fig. 1 and Additional file 1: Fig. S1A). During the austral winter, the coastal region is characterized by cold water, which follows a sharp frontal gradient, starting with the lowest temperatures inshore (~ 23 °C) and shifting toward higher temperatures offshore (25–27 °C; Fig. 1B). The elevated density of this narrow band of cold and saline (salinity = 35) water leads to a cross-shelf density gradient that results in the offshore transport of coastal water along the ocean floor (James et al. 2004; Mahjabin et al. 2020). This so-called denser shelf water cascade presently extends down to a depth of 150 m, transporting cold coastal waters over distances of > 50 km offshore (Mahjabin et al. 2020). During the austral summer months, strong solar heating results in high sea

surface temperatures (SSTs; > 30 °C) in the nearshore area, which gradually become lower further offshore (28–30 °C; Fig. 1A). The lateral and depth gradients of water temperature are less pronounced as compared with the austral winter months (Fig. 1B and Additional file 1: Fig. S1B). In addition, depth profiles display seawater salinities that are ~ 0.1 higher at the sea surface (< 40 m depth) as opposed to deeper waters during the austral summer (Additional file 1: Fig. S1C). This is opposite to the case in the austral winter months, when salinity increases steadily from 34.85 to 35.00 between the sea surface and 150 m depth (Additional file 1: Fig. S1C).

The water masses are mainly sourced by the Indonesian Throughflow (ITF), which originates in the Indo-Pacific Warm Pool and transports warm and oligotrophic seawater to the NWS. These waters form the Holloway Current, which feed into the Leeuwin Current around Cape Range (northwestern Australia; Pattiaratchi 2006; D'Adamo et al. 2009). Interannually, the oceanography of the NWS is modified by the El Niño–Southern Oscillation (ENSO). During El Niño events, the ITF and Holloway Current strengths are weakened due to modulations in the equatorial western Pacific wind stress (Feng et al. 2013). The weakened current system results in negative SST anomalies along the northwestern to western coast of Australia (Feng et al. 2004, 2013). In turn, La Niña events have been shown to trigger strong heatwaves in northwestern Australia, with water temperatures rising by several degrees (Feng et al. 2013; Tozuka et al. 2014; Zinke et al. 2015).

3 Materials and methods

This study is based on core material retrieved from IODP Sites U1461 (20°12.863′ S, 115°3.950′ E) and U1463 (18°57.918′ S, 117°37.422′ E). Site U1461 is located in the westernmost part of the NWS, 100 km northwest of Barrow Island at a water depth of 127 m (Fig. 1). Site U1463 is situated ~ 300 km northeast of Site U1461 in a slightly deeper water depth of 147 m (Fig. 1).

At Site U1461, samples were taken from the upper 10 m of holes U1461B and U1461C. The sediments are unlithified, olive to dark gray, skeletal wackestones to packstones, which were described in detail by Hallenberger et al. (2019). Samples from Site U1463 were collected from the upper 11.5 m of holes U1463B and U1463C. This section is broadly equivalent to Unit 1 as described in the IODP shipboard report (Gallagher et al., 2017a, b). Sediments in this section are creamy gray to light greenish gray, unlithified, wackestones to packstones, which were deposited in a neritic to hemipelagic environment. The calcium carbonate content is high (~ 87 wt%), with the microfossil assemblage consisting predominantly of pteropods and a variety of planktonic and miliolid

benthic foraminifers (Gallagher et al. 2017a, b). Bioturbation is moderate and only slight drilling disturbance occurs throughout the studied interval (Gallagher et al. 2017a, b). Measured total organic carbon (TOC) contents vary between 0.5 and 1.0 wt% at Site U1461 (Gallagher et al. 2017a, b) and 0.9–1.0 wt% at Site U1463 (Gallagher et al. 2017a, b). The depths of all samples are given as core composite depth below seafloor (CCSF) to account for differences in the individual depth scales of single holes. A total of 52 sample wedges filled with soft sediment (20 cm^3) were collected from Site U1461 ($n = 14$) and Site U1463 ($n = 38$). Each sample was subsequently wet sieved to separate the fine (< 63 μm) and coarse (> 63 μm) fraction. From the coarse fraction, pteropod shells of *H. inflatus,* benthic foraminiferal tests of the genus *Uvigerina* (*Uvigerina* spp.), and different planktic foraminiferal tests were handpicked.

3.1 Accelerator mass spectrometry ^{14}C dating

For Site U1461, a previously published age model was utilized to convert core depth into time before present (Hallenberger et al. 2019; Ishiwa et al. 2019). The chronology of Site U1463 is based on 10 accelerator mass spectrometry (AMS) radiocarbon (^{14}C) dates. Radiocarbon dating of a mixture of different planktic foraminifer species was performed by the Single Stage Accelerator Mass Spectrometer at the Atmosphere and Ocean Research Institute, The University of Tokyo, Japan (Yokoyama et al., 2019). Calibration to calendar years was undertaken with a Bayesian age modeling approach (Ramsey 2009) using the Marine20 database (Heaton et al. 2020). Utilizing the marine reservoir database (http://calib.org/marine/; Reimer and Reimer 2001), 10 known reservoir ages were averaged in a 1000 km radius (Bowman 1985; O'Connor et al. 2010). The resulting reservoir age is small (ΔR 57 ± 27), and thus, the local correction was set to zero. A continuous age model was calculated with Bchron, which is an age–depth modeling package implemented in "R" software (version 4.1.2) (Team 2018), using the algorithm of Haslett and Parnell (2008).

3.2 *Limacina* dissolution index

Pteropod shells were examined according to the *Limacina* dissolution index (LDX) (Gerhardt et al. 2000; Gerhardt and Henrich 2001). The LDX methodology involves the analysis of the surface of single *H. inflatus* shells. Depending on the preservation, each specimen is evaluated on a scale of 0–5, with 0 being a shell that is transparent and lustrous, with a perfect outer aragonite layer, and 5 being a shell that is opaque white in color, totally lusterless, and perforated, with extensive corrosion of the outer aragonite layer (Gerhardt and Henrich, 2001). For each sample, at least 10 shells of adult *H. inflatus* of a size

of ≥ 300 μm were assigned a preservation value based on optical microscopy observations. The LDX value for each sample was then calculated according to the following equation (Gerhardt et al. 2000; Gerhardt and Henrich 2001):

$$LDX = \sum (n_p \times p) / \sum n_p \tag{1}$$

where n_p is equal to the number of tests per preservation stage p (0–5) with the sum of n_p being at least 10. Dissolution along the shell surface was further evaluated using a scanning electron microscope (SEM; Keyence, VE 8800).

3.3 Stable carbon and oxygen isotopes

Stable carbon (δ^{13}C) and oxygen (δ^{18}O) isotopic compositions were determined for all the collected *H. inflatus* and *Uvigerina* spp. samples. Prior to measurement, each sample was cleaned in an ultrasonic bath to remove contamination. This process was repeated once with methanol and twice with ultra-pure deionized water. The quality of the cleaning process was subsequently evaluated by optical microscopy. In addition, a random subset of tests was checked for cementation by optical microscopy and with a SEM. A total of 10 specimens were pooled and crushed for subsequent measurement of δ^{13}C and δ^{18}O values. Measurements of the carbonate powders were conducted with a Thermo Fisher Scientific DeltaV Advantage mass spectrometer coupled to a ThermoQuest Kiel-III automated carbonate device at the Institute of Geology and Paleontology, Tohoku University, Japan. The samples (∼ 0.1 mg per sample) were reacted with 100% phosphoric acid at ∼ 72 °C. A value of 1.01025 was used as the factor to account for the δ^{18}O fractionation occurring during phosphoric acid digestion (Sharma and Clayton 1965). All results are reported in the δ notation in per mil (‰) calibrated to the NBS-19 international standard relative to the Vienna Pee Dee Belemnite (VPDB). The mean external error and reproducibility (1σ) were assessed by replicate measurements of an in-house carbonate standard (JCp-1; δ^{13}C = − 1.63‰ ± 0.03‰; δ^{18}O = − 4.71‰ ± 0.03‰) (Okai et al. 2004; Nakayama et al. 2008) and was determined to be low for both δ^{13}C (± 0.03‰) and δ^{18}O (± 0.05‰) values. Isotopic values determined on a control sample of 10 pteropods will deviate from the parent population of all pteropods in a single sediment sample. To estimate the uncertainty created by the selection of a subset of pteropods, we undertook repeat sampling and measurement of 10 pteropods from each parent population (i.e., coarse fraction of a sediment sample). The averaged measured deviations between both pteropod subsets were 0.12‰ for δ^{18}O and 0.07‰ for δ^{13}C.

3.4 Calcification depth of *H. inflatus*

Euthecosomatous pteropods have been found to precipitate aragonite close to oxygen isotope equilibrium ($\delta^{18}O_{eq}$) with ambient seawater (Grossman et al. 1986, Almogi-Labin et al. 1991, Fabry and Deuser 1992, Juranek et al. 2003, Keul et al. 2017). For *H. inflatus*, differences between the calculated $\delta^{18}O_{eq}$ and $\delta^{18}O$ values measured in shells have been shown to be minor, ranging from 0 to 0.1‰ (Fabry and Deuser 1992). Based on this observation, the depth of calcification of *H. inflatus* can be determined by comparing the $\delta^{18}O$ measured in *H. inflatus* with $\delta^{18}O_{eq}$ depth profiles of the ambient seawater (Grossman et al. 1986; Wall-Palmer et al. 2018). $\delta^{18}O_{eq}$ profiles were approximated as a function of water temperature and the oxygen isotopic composition of seawater ($\delta^{18}O_{sw}$; Grossman and Ku 1986, Juranek et al. 2003, Keul et al. 2017), where $\delta^{18}O_{sw}$ was determined based on

a regional correlation between $\delta^{18}O_{sw}$ and seawater salinity (S; Pei et al. 2021a, b):

$$\delta^{18}O_{sw} = -11.66 + 0.34 \times S. \qquad (2)$$

Seasonal profiles of water temperature and salinity at Sites U1461 (Station 273179) and U1463 (Station 278667) were derived from the World Ocean Atlas 2018 (Locarnini et al. 2018). $\delta^{18}O_{eq}$ was then calculated based on a linear regression devised for generic aragonitic marine organisms, which calcify in equilibrium with $\delta^{18}O_{sw}$ (Böhm et al. 2000):

$$T\left(^{\circ}C\right) = 20 - 4.42 \times \left(\delta^{18}O_{eq} - \delta^{18}O_{sw}\right). \qquad (3)$$

The temperature–$\delta^{18}O$ relationship devised by Böhm et al. (2000) combines several sources of biogenic and synthetic aragonite data (Tarutani et al. 1969; Grossman and Ku 1986; Rahimpour-Bonab et al. 1997; Böhm et al. 2000), which thus extends the temperature window and reduces the overall error present in previous studies (Böhm et al. 2000). It has been successfully applied to calculate water temperatures from *H. inflatus* shells and was therefore favored over other calibrations in the literature (Oakes et al. 2021). This correlation was also preferred over the only existing species-specific correlation for *H. inflatus* (Keul et al. 2017), as it includes the high water temperatures typical of the NWS (Böhm et al. 2000).

3.5 Conversion of ice volume-corrected oxygen isotope data to temperature

The regression of Böhm et al. (2000) was further used to estimate past changes in water temperature by replacing the $\delta^{18}O_{eq}$ values with the $\delta^{18}O$ values measured in the *H. inflatus* shells using Eq. (3). Since there are no data on the past $\delta^{18}O_{sw}$ or salinity values available for the NWS, $\delta^{18}O_{sw}$ was approximated based on modern values (Additional file 1: Fig. S1D). Calculated $\delta^{18}O_{sw}$ values range from 0.15 to 0.25‰, with limited fluctuations with depth or season (Additional file 1: Fig. S1D). Based on this distribution, we set the $\delta^{18}O_{sw}$ value used in the temperature calculations to be equivalent to the overall mean observed at both sites (mean = 0.21‰).

Past seafloor water temperatures recorded at Site U1463 were reconstructed based on the $\delta^{18}O$ values of the benthic foraminifera *Uvigerina* spp. using the regression of Marchitto et al. (2014):

$$T\left(^{\circ}C\right) = \frac{0.245 - \sqrt{0.045461 + 0.0044\left(\delta^{18}O - \delta^{18}O_{sw} - 0.47\right)}}{0.0022}. \qquad (4)$$

To account for the $\delta^{18}O$ offset caused by changing ice volume, measured values for *H. inflatus* and *Uvigerina* spp. were adjusted by -0.1‰ for each 10 m of sea-level fall (Shackleton and Opdyke, 1973), following the global Quaternary sea-level curve of Lambeck et al. (2014).

3.6 Conversion of carbon isotope data to carbonate ion concentrations

The $\delta^{13}C$ values of pteropods are inversely correlated with the carbonate ion concentration ($[CO_3^{2-}]$) of seawater (Juranek et al. 2003; Keul et al. 2017). In this study, $[CO_3^{2-}]$ was calculated based on the $\delta^{13}C$ values of *H. inflatus* using the species-specific correlation presented by Keul et al. (2017):

$$\text{carbonate ion concentration} = \frac{\delta^{13}C - 3.067}{-0.01}. \qquad (5)$$
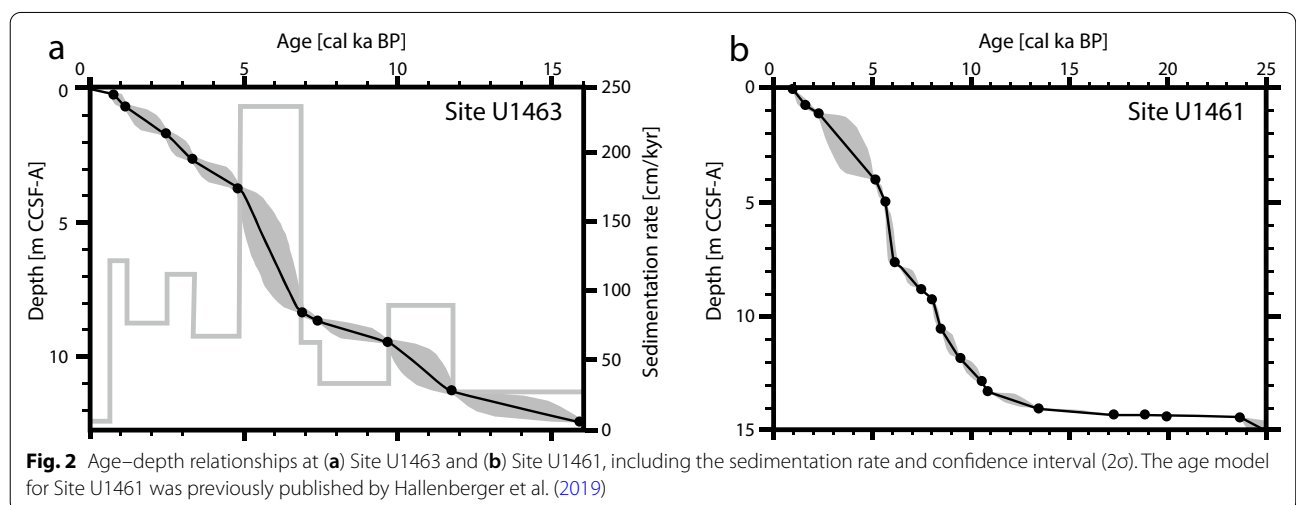
4 Results

4.1 Age model for site U1463

Radiocarbon ages acquired for Site U1463 are provided in Table 1 and Fig. 2. The chronological profile suggests that the upper 12 m of core corresponds to the last 16 kyr (Fig. 2). Between 16 and 7 ka, sedimentation rates were comparatively low (30–90 cm/kyr). After 7 ka, the sedimentation rate exhibited a substantial increase (60–230 cm/kyr), with a marked peak observed between 7 and 5 ka (230 cm/kyr). Subsequently, relatively low

Table 1 Age results of Site U1463

Laboratory Code	Sample Name	Depth CSF-A [m]	Depth CCSF-A [m]	Radiocarbon age [year BP]	Calendar age [cal year BP] 95% highest density regions	
YAUT-034202	356-U1463B-1H-1A 0/4	0.02	0.02	1216 ± 37	501	730
YAUT-034203	356-U1463B-1H-1A 68/72	0.7	0.7	1775 ± 34	1029	1297
YAUT-034204	356-U1463B-1H-2A 18/22	1.7	1.7	2887 ± 31	2326	2662
YAUT-034205	356-U1463B-1H-2A 118/122	2.7	2.7	3632 ± 29	3215	3514
YAUT-034206	356-U1463B-1H-3A 68/72	3.7	3.7	4789 ± 29	4689	5034
YAUT-051514	356-U1463C-2H-3A 17/21	7.31	8.31	6552 ± 53	6635	7026
YAUT-055628	356-U1463C-2H-3A 55/59	7.69	8.69	7136 ± 28	7306	7563
YAUT-056104	356-U1463C-2H-3A 130/134	8.44	9.44	9143 ± 36	9522	9883
YAUT-056105	356-U1463C-2H-5A 17/21	10.31	11.31	10,626 ± 47	11,506	11,997
YAUT-051515	356-U1463C-2H-5A 130/134	11.44	12.44	13,914 ± 85	15,667	16,269

Calibration of calendar years was based on a Bayesian age modeling approach (Ramsey, 2009) using the Marine20 database (Heaton et al., 2020). Depth of individual samples is given as core depth below sea floor (CSF-A) and core composite depth below sea floor (CCSF-A), as defined by the IODP Depth Scale Terminology (IODP-MI 2011). Calendar ages are represented by the lower and upper boundary of the highest density region

Fig. 2 Age–depth relationships at (**a**) Site U1463 and (**b**) Site U1461, including the sedimentation rate and confidence interval (2σ). The age model for Site U1461 was previously published by Hallenberger et al. (2019)

sedimentation rates characterized the uppermost part of the studied core, where only 2 cm of sediment represents the last 600 yr (3 cm/kyr). This may be the result of a technical issue that is typical of IODP drilling operations, whereby the uppermost sediment in a core is often lost.

4.2 *Limacina* dissolution index
Pteropod data for Sites U1461 and U1463 are shown in Fig. 3 and listed in Additional file 1: Tables S1–S2. Pteropod preservation at both sites ranged between pristine (LDX = 0) and excellent (LDX = 1), with LDX values never exceeding 1 (Fig. 3). At Site U1461, the pteropods were pristine (LDX = 0) throughout the studied core section, without any notable trends or changes (Fig. 3). At Site U1463, the pteropods were mostly pristine, with little to no evidence of dissolution (Fig. 4A). An

exception was found in an interval deposited between 8 and 6 ka, where the average preservation state of the pteropods was slightly deteriorated (LDX = 1; Fig. 3). Shells occurring within this interval were often partially opaque white or slightly cloudy, indicating initial dissolution of the shell surface (Fig. 4B). In part, this dissolution removed the outer layer of the pteropod shells, exposing the underlying rod-like internal structure (Fig. 4C–D).

4.3 Oxygen isotopes and water temperatures
Measured $\delta^{18}O$ values are shown in Fig. 3 and listed in Additional file 1: Tables S1–S2. Pteropod $\delta^{18}O$ values displayed a clear trend over time at Site U1463 (Fig. 3). Prior to 10 ka, the $\delta^{18}O$ values were elevated as compared with the rest of the section, with $\delta^{18}O = 0.2–0.8‰$
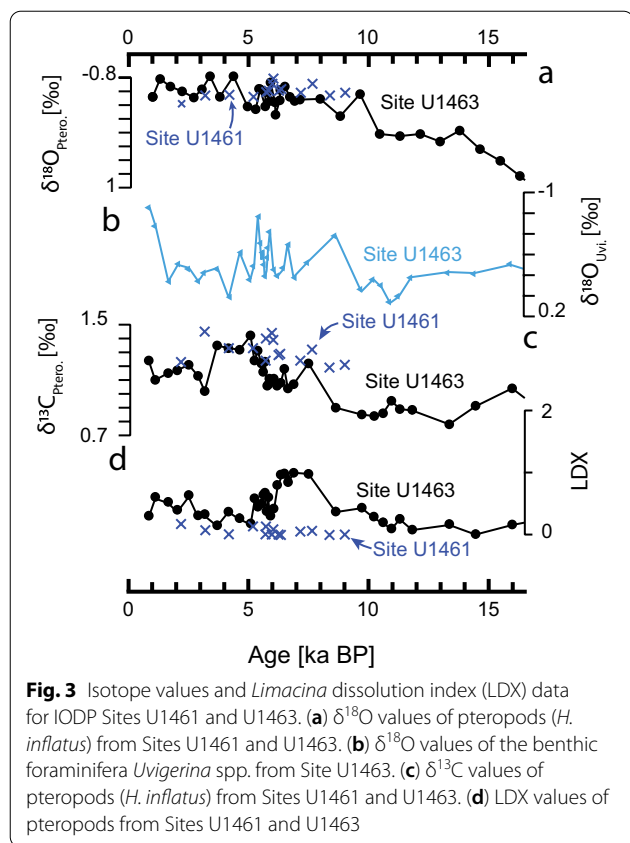
Fig. 3 Isotope values and *Limacina* dissolution index (LDX) data for IODP Sites U1461 and U1463. (**a**) $\delta^{18}O$ values of pteropods (*H. inflatus*) from Sites U1461 and U1463. (**b**) $\delta^{18}O$ values of the benthic foraminifera *Uvigerina* spp. from Site U1463. (**c**) $\delta^{13}C$ values of pteropods (*H. inflatus*) from Sites U1461 and U1463. (**d**) LDX values of pteropods from Sites U1461 and U1463

(mean = 0.4‰). At *ca*. 10 ka, the $\delta^{18}O$ values decreased rapidly from 0.2‰ to -0.4‰ (Fig. 3). Pteropods of younger age have consistently low $\delta^{18}O$ values of -0.6‰ to -0.2‰ (mean = -0.3‰). The $\delta^{18}O$ values for *H. inflatus* from Site U1461 are largely the same as those from Site U1463 within the selected age segment, with values varying between -0.7‰ and -0.2‰ (mean = -0.4‰).

Water temperatures calculated from pteropods at both sites fluctuate between 21.5 and 24.2 °C, with an average temperature of 22.8 °C (Fig. 5B; Additional file 1: Tables S3–S4). As opposed to the $\delta^{18}O$ profiles, there were no discernable trends or systematic changes in water temperature over time or between the two sites (Fig. 5B).

$\delta^{18}O$ values of *Uvigerina* spp. from Site U1463 vary between -0.9‰ and 0.0‰ (mean = -0.6‰) without any discernible trends over time (Fig. 3; Additional file 1: Table S2). Calculated temperatures were highest (26.7 °C) for the oldest measured sample at 16 ka, and decreased steadily until the present-day, when water temperatures at Site U1463 were ~ 18 °C (Fig. 5C).

4.4 Carbon isotopes and carbonate ion concentrations
$\delta^{13}C$ values of pteropods from Sites U1461 and U1463 are listed in Additional file 1: Tables S1 and S2 and

shown in Fig. 3. In general, the $\delta^{13}C$ values of *H. inflatus* vary between 0.8 and 1.5‰ (mean = 1.2‰). A direct comparison between values obtained from equivalent age ranges at both sites revealed a statistically significant (student t-test; $p < 0.05$) higher mean for Site U1461 (mean = 1.3‰) as compared with Site U1463 (mean = 1.1‰). $\delta^{13}C$ values of pteropods from Site U1461 exhibit no clear trends over time, with $\delta^{13}C$ ratios ranging between 1.2 and 1.5‰ (mean = 1.3‰). At Site U1463, the $\delta^{13}C$ values vary from 0.8 to 1.4‰ (mean = 1.1‰), with the values increasing significantly ($p < 0.05$) after 8.5 ka (Fig. 3). Prior to 8.5 ka, the $\delta^{13}C$ values were comparatively low (0.8–1.0‰; Fig. 3). At *ca*. 8.5 ka, $\delta^{13}C$ values display an abrupt increase from 0.9 to 1.2‰ between two data points (Fig. 3). Thereafter, the $\delta^{13}C$ values remain high (1.0–1.4‰).

Calculated $[CO_3^{2-}]$ for Sites U1461 and U1463 are listed in Additional file 1: Tables S3 and S4, respectively. The $[CO_3^{2-}]$ profile displays an inverse trend over time as compared with the measured $\delta^{13}C$ profiles (Fig. 6A). Prior to 8.5 ka, calculated values for Site U1463 are consistently high, with $[CO_3^{2-}]$ of 200–230 μmol/kg of seawater (sw) (Fig. 6A). At *ca*. 8.5 ka, $[CO_3^{2-}]$ decreased notably by almost 40 μmol/kg sw (Fig. 6A). Following this decrease, $[CO_3^{2-}]$ fluctuated but remained at lower levels as compared with pre-8.5 ka, with values of 160–200 μmol/kg sw (Fig. 6A). At Site U1461, calculated $[CO_3^{2-}]$ were consistently slightly lower ($p < 0.05$) as compared with those at Site U1463, with values of 160–190 μmol/kg sw (Fig. 6A).

5 Discussion
5.1 Calcification depth of *H. inflatus*
A comparison between the $\delta^{18}O_{eq}$ profiles and $\delta^{18}O$ values measured in *H. inflatus* reveals that the annual average calcification depths were 95–140 m (Fig. 7). Seasonal changes in $\delta^{18}O_{eq}$ are minor, with shallower calcification depths for the summer months (85–130 m) as compared with the winter months (115–155 m; Fig. 7). These results are indicative of slightly deeper calcification as compared with most open marine *H. inflatus* records, which have estimated calcification depths to be 50–100 m (Fabry and Deuser 1992; Jasper and Deuser 1993; Keul et al. 2017; Oakes et al. 2021). Notably, the calcification depths are at the shallow end of the range proposed by Juranek et al. (2003) for *H. inflatus* from the Sargasso Sea (50–650 m).

Past seawater temperatures calculated from the $\delta^{18}O$ values of *H. inflatus* range between 21.5 and 24.2 °C, with little apparent change from 16 ka onward (Fig. 5). This is inconsistent with regional records from northwestern Australia (Spooner et al. 2011; De Deckker et al. 2014; Pei et al. 2021a, b) and the Timor Sea (Xu et al. 2008; Sarnthein et al. 2011; Pei et al. 2021a, b), which indicate an
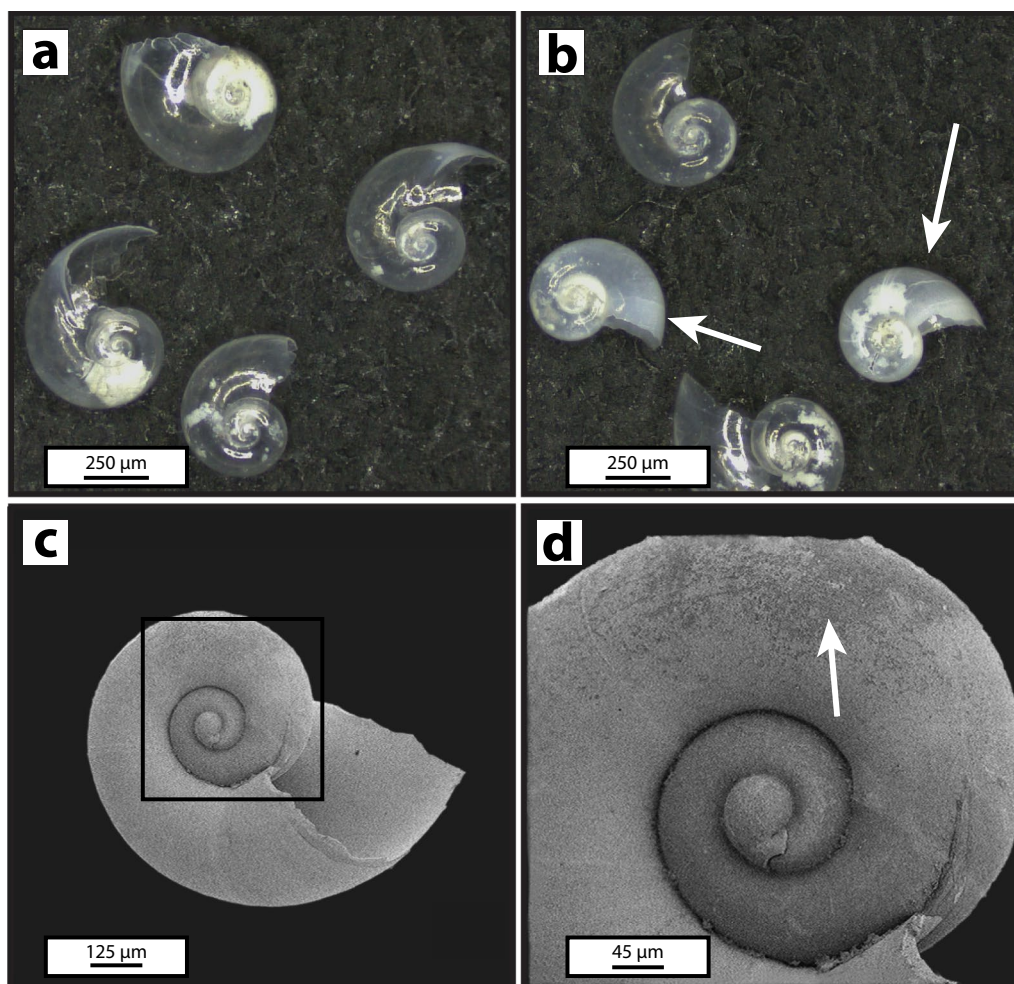
Fig. 4 Optical microscopy and SEM images of selected *H. inflatus* samples. (**a**) Most pteropods in the studied core material are very well preserved (LDX = 0), including lustrous and transparent shells (Site U1463; 12 ka). (**b**) The preservation of some shells from Site U1463 (6–8 ka) exhibits slight deterioration (LDX = 0–1). Single shells partly have an opaque milky white color or a cloudy appearance (white arrow) (Site U1463; 7 ka). (**c**) SEM image of a slightly corroded pteropod. The black square indicates the location of (d) (Site U1463; 7 ka). (**d**) Dissolution of a pteropod as evidenced by the rough surface of part of the shell (white arrow) (Site U1463; 7 ka)

increase in SSTs ranging between 2 and 4 °C from 16 ka to the present. However, records from water depths of > 100 m or from the thermocline level indicate there was no notable increase in temperature during the same period (Fig. 5F–G). This is consistent with the estimated calcification depths being below 100 m (Fig. 7).

Temperatures at a depth equivalent to the seafloor, as recorded by the benthic foraminifera *Uvigerina* spp., display a clear trend over time, with values decreasing considerably from 16 ka (27 °C) to 8.6 ka (20 °C; Fig. 5C). After 8.6 ka, the seafloor temperatures are largely stable, with values equivalent to those measured at the present-day at Site U1463 (Additional file 1: Fig. S1). The post-glacial decrease in seawater temperature was likely the result of a progressive rise in

sea level (Fig. 5A). Site U1463 is presently situated at a water depth of 147 m and was characterized by shallow-marine inner ramp conditions (< 40 m) prior to the post-glacial transgression (Fig. 5A). The shelf surrounding Site U1463 was likely affected by the strong seasonality in seawater temperatures on the coastal NWS (Fig. 1A, B). This is particularly relevant for *Uvigerina* spp., because it can display a seasonal bias based on the availability of nutrients (Ohga and Kitazato 1997; Fontanier et al. 2003; Scourse et al. 2004). On the NWS, nutrient availability is largest during the austral summer months (Hallegraeff and Jeffrey 1984; Rochford 1988; James et al. 2004), implying a spike in *Uvigerina* spp. abundance during the austral summer months. As such, the δ^{18}O values of *Uvigerina* spp. likely record
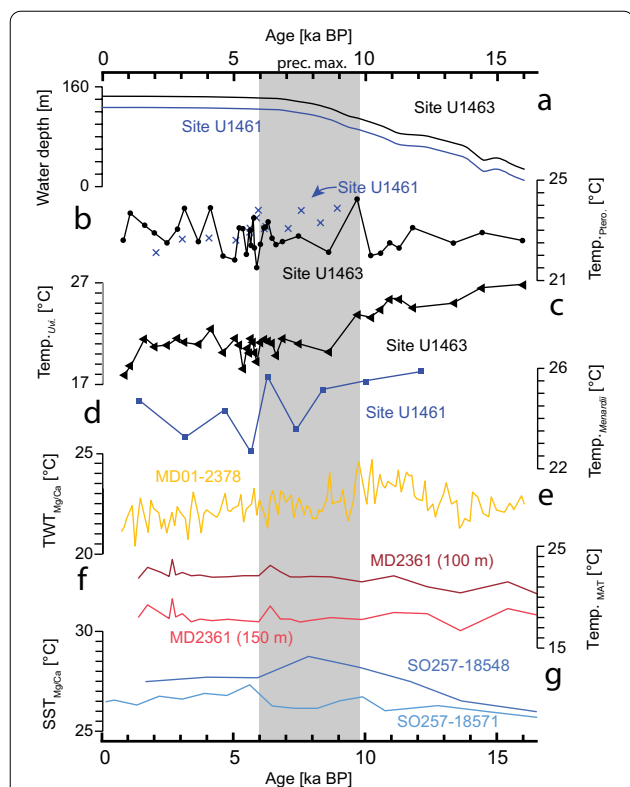
Fig. 5 Water temperature proxies at Sites U1461 and U1463 as compared with regional data. The gray band indicates a precipitation maximum on the NWS (Hallenberger et al. 2019; Ishiwa et al. 2019). (**a**) Paleo-water depth at both studied sites based on the sea-level curve of Lambeck et al. (2014). The relative sea level at Sites U1461 and U1463 was not corrected for isostatic deformation. (**b**) Water temperature based on the $\delta^{18}O$ values of *H. inflatus*. (**c**) Water temperature calculated from $\delta^{18}O$ data for *Uvigerina* spp. at Site U1463. (**d**) $\delta^{18}O$ data for the planktic foraminifera *G. menardii* (Courtillat et al. 2020) used to calculate past changes in upper thermocline water temperatures at Site U1461. (**e**) Past variations in thermocline water temperatures based on the Mg/Ca ratio of *P. obliquiloculata* at Site MD01-2378 (Xu et al. 2008). (**f**) Water temperature record from the North West Cape of Australia (MD-2361) at 100 and 150 m depth based on the modern analogue technique (Spooner et al. 2011). (**g**) Sea surface temperature changes based on the Mg/Ca ratios of *G. ruber* in the Timor Sea (Site SO257-18548) and offshore of northwestern Australia (Site SO257-18571; Pei et al., 2021b)

Fig. 6 Selected downcore records of regional and global proxies compared with data from IODP Sites U1461 and U1463. The gray band indicates a regional precipitation maximum on the NWS (Hallenberger et al. 2019; Ishiwa et al. 2019). (**a**) Carbonate ion concentration calculated from $\delta^{13}C$ values of pteropods. (**b**) Atmospheric CO_2 concentration determined from the Dome Concordia (Antarctica) ice core (Monnin et al. 2001). (**c**) *Limacina* dissolution index (LDX) for pteropods from Sites U1461 and U1463. (**d**) The log ratio of Ti/Ca, which is a proxy for arid (low values) and humid (high values) conditions in northwestern Australia. Site U1461 (Hallenberger et al. 2019) records the onset of humid conditions after *ca*. 10 ka

high, nearshore, austral summer water temperatures during lowstand conditions (Fig. 1A). During the post-glacial rise in sea level, Site U1463 became progressively more distal and was thus less affected by the strong seasonal fluctuations in nearshore water temperatures (Fig. 1A, B). This is clearly reflected by the present-day conditions, which indicate comparatively stable water temperatures at Site U1463 on the seafloor throughout the year (Additional file 1: Fig. S1A).
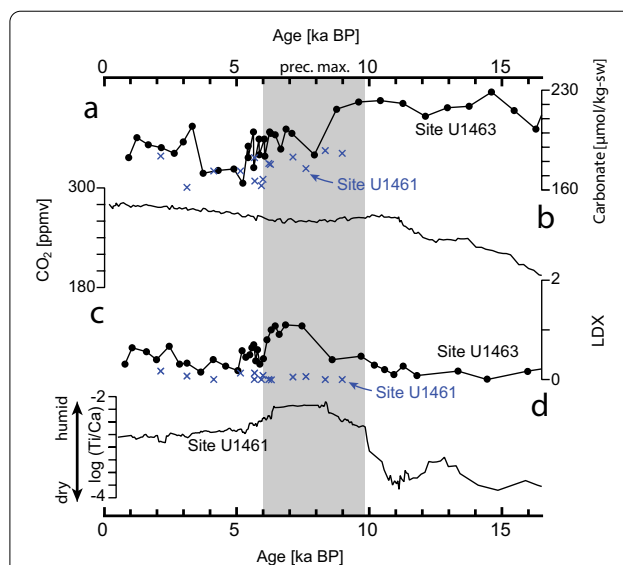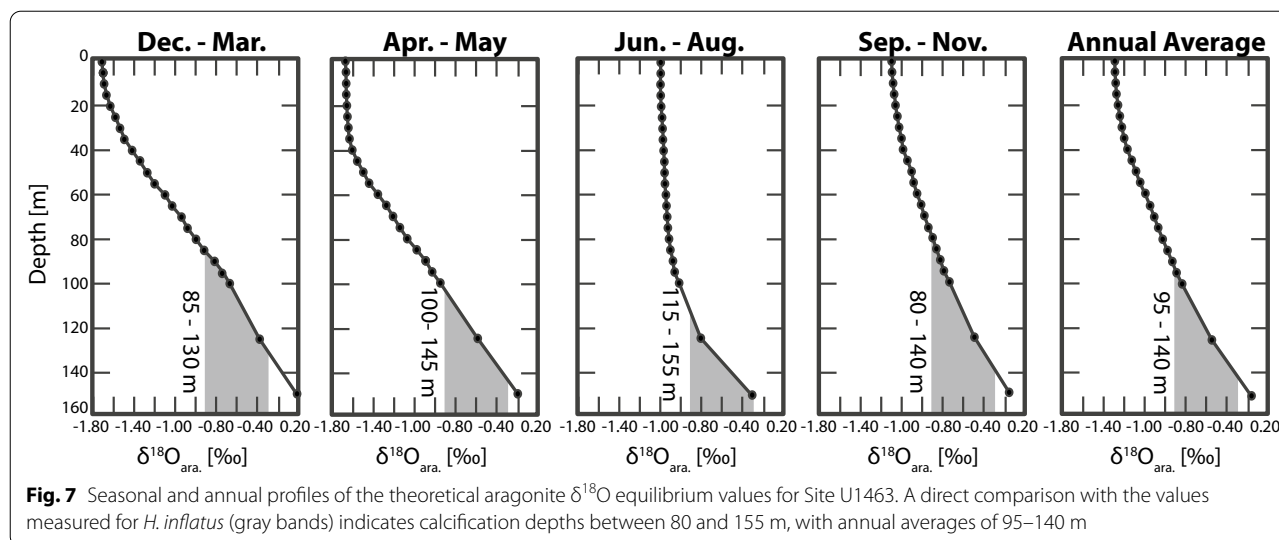
In comparison, *H. inflatus* calcified at considerably lower temperatures than *Uvigerina* spp. from 16 to 10 ka (Fig. 5B, C). This temperature difference decreased steadily until 10 ka, after which the pteropods display a constant 2 °C offset toward higher temperatures as compared with *Uvigerina*-based seafloor temperatures (Fig. 5B, C). This can be interpreted to be the result of a post-glacial rise in sea level. While the calcification depth of benthic *Uvigerina* spp. increased, *H. inflatus* appeared to calcify at constant temperatures regardless of the sea level (Fig. 5B). Given that depth is the main control on seawater temperature across the shelf, it may be concluded that until *ca.* 10 ka *H. inflatus* calcified at greater depths as compared to the Site U1463 seafloor and were thus sourced from further offshore. This interpretation is supported by the comparatively small amount of pteropods present in this section of the core (Gallagher et al. 2017a, b). After 10 ka, the pteropods calcified in warmer and shallower water as compared with the seafloor of Site U1463 (Fig. 5).

At Site U1461, an existing $\delta^{18}O$ record for the planktic foraminifera *Globorotalia menardii* (Courtillat et al. 2020) was converted into water temperatures using the

Fig. 7 Seasonal and annual profiles of the theoretical aragonite $\delta^{18}O$ equilibrium values for Site U1463. A direct comparison with the values measured for *H. inflatus* (gray bands) indicates calcification depths between 80 and 155 m, with annual averages of 95–140 m

regression presented by Spero et al. (2003). The resulting temperatures are 22.6–26 °C, with no discernible trend over time (Fig. 5D). *Globorotalia menardii* calcifies primarily at the upper thermocline level (Sautter and Thunell 1991; Ravelo and Fairbanks 1992; Niebler et al. 1999; Spero et al. 2003; Wejnert et al. 2010), with a limited seasonal flux in tropical and subtropical waters (Jonkers and Kučera 2015; Venancio et al. 2017). On the present-day NWS, the depth of the thermocline can be approximated from the vertically and seasonally resolved World Ocean Atlas seawater temperature database (Locarnini et al. 2018). The thermocline is defined here as the zone of highest depth-dependent gradient in seawater temperature, which is at its shallowest between December–May (40–100 m; Additional file 1: Fig. S1B). In comparison, the thermocline is only weakly developed between June–November, where substantial increases in the temperature gradient only become evident below 100 m depth (Additional file 1: Fig. S1B). This observation is consistent with previous studies, which suggested that the water column is well-stratified during the austral summer and strongly mixed during the austral winter (Hallegraeff and Jeffrey 1984; James et al. 2004). On average, *G. menardii* records significantly ($p < 0.05$) higher (+1.6 °C) seawater temperatures as compared with *H. inflatus* (Fig. 5). The constant offset in temperatures between both archives indicates that *H. inflatus* calcifies in deeper waters as compared with the upper thermocline dwelling *G. menardii*. The lack of variability of *G. menardii* $\delta^{18}O$ values further supports the assumption that the water temperatures at the thermocline level remained largely unaffected by post-glacial increases in temperature.

5.2 Development of shallow-marine aragonite saturation on the NWS

$\delta^{13}C$ values of the pteropods from Site U1463 record a clear trend over time, with values increasing markedly after 8.5 ka (Fig. 3). This increase is broadly coeval with a fundamental change in shallow-marine carbonate sedimentation on the NWS (Hallenberger et al. 2019). After 10 ka, the dominant mode of carbonate production across large parts of the NWS changed from inorganic aragonite to skeletal calcite (James et al. 2004; Dix et al. 2005; Hallenberger et al. 2019). This change was proposed to be the result of a more humid climate caused by the onset of the Australian Summer Monsoon, which in turn led to a decrease in the saturation state of aragonite (Hallenberger et al. 2019; Ishiwa et al. 2019). The saturation state of aragonite (Ω_{arag}) is closely linked to the $[CO_3^{2-}]$, which in turn is inversely correlated with the $\delta^{13}C$ values of *H. inflatus* (Juranek et al. 2003; Keul et al. 2017). As such, both the $\delta^{13}C$ values of the pteropods and sedimentary composition indicate there was a change in seawater Ω_{arag} at a similar time on the NWS.

In addition, the $\delta^{13}C$ values of pteropod shells can be influenced by several factors, which can obscure any potential signal caused by variations in $[CO_3^{2-}]$. To avoid any misinterpretation, possible alternative factors influencing the $\delta^{13}C$ values are now briefly discussed.

Fluctuations in riverine influx can substantially alter the chemical and isotopic composition of tropical coastal waters (Zeebe and Wolf-Gladrow 2001; Moyer and Grottoli 2011; Utami et al. 2021). A previous study suggested an abrupt increase in riverine influx across the NWS after 10 ka (Hallenberger et al. 2019). This is not reflected by the $\delta^{13}C$ values measured at Sites U1461 and U1463. In

particular, at Site U1463, the $\delta^{13}C$ values were higher rather than lower after 10 ka, and therefore opposite to what would be expected from a potential riverine influx (Fig. 6).

Enhanced productivity can result in higher $\delta^{13}C$ values of dissolved inorganic carbon ($\delta^{13}C_{DIC}$), which could affect the $\delta^{13}C$ values of the pteropods shells (Lazar and Erez 1992). However, published data for offshore northwestern Australia suggest that productivity remained largely unaffected during the last glacial to interglacial transition (Martínez et al. 1999, Spooner et al. 2011), with uniformly oligotrophic conditions present during the last glacial as well as in the Holocene (Murgese and De Deckker 2007). This is consistent with limited sampling of TOC at Site U1463, which did not reveal an increase during the last glacial period as compared with the present-day interglacial (Gallagher et al., 2017a, b).

Finally, there were global shifts to lower $\delta^{13}C_{DIC}$ values of ocean waters during glacial stages as compared with interglacial stages caused by differences in the terrestrial storage capacity of ^{13}C (Curry et al. 1988; Duplessy et al. 1988; Peterson et al. 2014). This mechanism is proposed to modify the $\delta^{13}C_{DIC}$ values of the entire ocean by up to 0.5‰ (Curry et al. 1988; Duplessy et al. 1988; Peterson et al. 2014). However, in shallow tropical oceans (< 500 m depth), glacial to interglacial changes are more limited, with cited values averaging out at 0.0‰ (McGee et al. 2007; Broecker and McGee 2013).

After 8.5 ka, the $[CO_3^{2-}]$ derived from the $\delta^{13}C$ values of *H. inflatus* display no significant changes and thus likely reflect the modern conditions on the NWS. Both deep water and shelf records of climate display a slight increase in aridity following ~ 6 ka (Kuhnt et al., 2015; Ishiwa et al., 2019; Hallenberger et al., 2019). This trend is not reflected in $[CO_3^{2-}]$ values (Fig. 6), indicating a potential lack in sensitivity of *H. inflatus* proxy data. Values for present-day $[CO_3^{2-}]$ on the NWS have been estimated using the python toolbox PyCO2SYS (Humphreys et al. 2020) and were compared with those determined from *H. inflatus.* PyCO2SYS solves the carbonate system for all major components, including $[CO_3^{2-}]$, if two out of nine defining parameters as well as temperature and salinity are available (Humphreys et al. 2020). In this study, the carbonate system was resolved by utilizing a combination of alkalinity (GLODAP Station 36379; Key et al. 2004), pH (GLODAP Station 36379; Key et al. 2004), salinity (WOA Station 278667; Zweng et al. 2019), and *H. inflatus* based-seawater temperatures (Fig. 5; Additional file 1: Tables S3–S4). The upper and lower boundaries of the water depth for which the $[CO_3^{2-}]$ was calculated are defined by the estimated calcification depths of *H. inflatus* (95–140 m). Using these constraints, we calculated a modern $[CO_3^{2-}]$ of 158 and 211 μmol/kg sw for 140 and 95 m water depth, respectively. In comparison, $[CO_3^{2-}]$ determined from *H. inflatus*

at ≤ 8.5 ka are 160–200 μmol/kg sw, with an average of 185 μmol/kg sw (Fig. 6; Additional file 1: Tables S3–S4). Therefore, the calculated present-day $[CO_3^{2-}]$ are the same as those determined from the *H. inflatus* data.

5.3 *Limacina* dissolution index as a shallow-marine proxy

The LDX was originally utilized to track the location and past variations of the aragonite lysocline (Gerhardt et al. 2000; Gerhardt and Henrich 2001). Based on its depth, pteropods undergo strong corrosion at the sediment–water interface (Gerhardt and Henrich 2001). Recent research has expanded the application of the LDX to glacial to interglacial changes in Ω_{arag} of ocean waters caused by fluctuations in atmospheric CO_2 (Wall-Palmer et al. 2013, 2014; Sreevidya et al. 2019) or changes in water mass properties (Klöcker et al. 2006). Better preservation typically characterizes glacial stages, when lower atmospheric CO_2 results in higher Ω_{arag} (Wall-Palmer et al. 2013, 2014). Unlike its original application, dissolution is proposed to occur "in-life" due to the pteropods interacting with surrounding ocean water (Wall-Palmer et al. 2013, 2014). Comparable features have been reported for modern pteropods, where in-life shell dissolution has been linked to anthropogenic changes in atmospheric CO_2 (Orr et al. 2005; Roger et al. 2012).

For shelf sediments offshore of northwestern Australia, LDX values remain low regardless of the post-glacial increase in global atmospheric CO_2 (Fig. 6). The pristine condition of most pteropods implies a near absence of in-life dissolution or dissolution at the sediment–water interface. LDX values have also been used to track the intensity of aragonite dissolution in marine porewaters during shallow burial (Reuning et al. 2022). They have shown that dissolution of relatively Sr-rich aragonite, as indicated by increased LDX values, leads to a concomitant increase in Sr ion concentrations in the porewater. The slight increase of LDX values at *ca.* 8–6 ka (Fig. 3) was not associated with an excess Sr concentration in a porewater sample from this interval (Gallagher et al., 2017a, b). As such, there is no evidence for aragonite dissolution during burial in the studied section. Instead, the overall excellent pteropod preservation (Fig. 6) indicates that the shallow-marine environment of the NWS was characterized by protracted elevated Ω_{arag}. This is supported by the strong aragonite supersaturation on the modern NWS ($\Omega_{arag} \approx 4$) (Roger et al. 2012). In the past, reduced amounts of atmospheric CO_2 (Monnin et al. 2001), as well as elevated regional aridity (Hallenberger et al. 2019; Ishiwa et al. 2019), are likely to have resulted in even higher levels of supersaturation.

An exception was recorded for the period between 8 and 6 ka, when the preservation of pteropods was slightly deteriorated at Site U1463 (Fig. 6). This was broadly coeval with the recorded decrease in carbonate ion concentrations

(*ca.* 8.5 ka), implying that the lower $[CO_3^{2-}]$ may have affected shell preservation (Fig. 6). The duration of this period matches a phase of elevated humidity reported for the NWS and Western Australia (Van der Kaars et al. 2006; Hallenberger et al. 2019; Ishiwa et al. 2019; Pei et al. 2021a, b). It is possible that the associated increase in riverine influx and precipitation led to a decrease of the Ω_{arag} in the shelf waters, resulting in the slight corrosion of the pteropods formed in this period. After *ca.* 6 ka, the climate proxies record a gradual return to more arid conditions in northwestern Australia (Kuhnt et al. 2015; Hallenberger et al. 2019; Ishiwa et al. 2019). Consequently, pteropod preservation again became pristine. However, such interpretations should be made with caution as there are no similar trends recorded for pteropods at Site U1461 (Fig. 6).

6 Conclusions

A 16-kyr-long sedimentary record from the NWS was studied to determine past ocean water conditions, based on different proxy records from *H. inflatus*. $\delta^{18}O$-based calcification depths indicate that *H. inflatus* records a shallow-marine shelf signal, with comparable conditions between 95 and 140 m depth on the modern NWS. A direct comparison with different archives further revealed that *H. inflatus* calcified at lower temperatures than the upper thermocline dwelling *Globorotalia menardii*, but at higher temperatures (post-10 ka) than benthic foraminifera of the genus *Uvigerina*. This places lower (Site U1463 seafloor; 147 m depth) and upper (upper thermocline) boundaries on the calcification depth of *H. inflatus*. Based on these conditions, a preferential calcification in the nutrient-rich thermocline is proposed for the NWS. This conclusion is supported by an overall lack of temperature changes since 16 ka, which is analogous to regional foraminifera-based thermocline records.

Past variations in shallow-marine $[CO_3^{2-}]$ and the saturation state of aragonite were tracked using the LDX and $\delta^{13}C$ values of *H. inflatus*. LDX values indicate limited changes during the last 16 kyr, irrespective of the coeval global increase in atmospheric CO_2 and/or regional fluctuations in the hydrological cycle. As such, it is likely that the sensitivity of the LDX proxy is not sufficient to record glacial to interglacial changes in the saturation state of aragonite (Ω_{arag}) in a highly supersaturated shallow-marine environment, such as the NWS. In comparison, the $\delta^{13}C$ values of *H. inflatus* showed a post-glacial decrease in $[CO_3^{2-}]$ at *ca.* 8.5 ka. This can be linked to the proposed onset of monsoonal rainfall and humid conditions on the NWS. It further coincides with the previously recorded shelf-wide cessation of inorganic aragonite production. Our study supports the hypothesis that climate-related changes in aragonite saturation states

were responsible for the cyclical change in carbonate facies deposition across the extensive ramp system.

Abbreviations

NWS: Northwest Shelf of Australia; LDX: *Limacina* Dissolution index; IODP: International Ocean Discovery Program; ITF: Indonesian Throughflow; SST: Sea surface temperature; CSF-A: Core depth below seafloor; CCSF-A: Core composite depth below seafloor; AMS: Accelerator mass spectrometry; $\delta^{13}C$: Carbon isotope ratio; $\delta^{18}O$: Oxygen isotope ratio; $\delta^{18}O_{eq}$: $\delta^{18}O$ of carbonates precipitating in equilibrium with seawater; $\delta^{18}O_{sw}$: $\delta^{18}O$ of seawater; $[CO_3^{2-}]$: Carbonate ion concentration; sw: Seawater; Ω_{arag}: Saturation state of aragonite; $\delta^{13}C_{DIC}$: $\delta^{13}C$ of dissolved inorganic carbon (DIC).

Supplementary Information

The online version contains supplementary material available at https://doi.org/10.1186/s40645-022-00507-1.

Additional file 1: Table S1. *Limacina* dissolution index and carbon and oxygen isotope data for pteropods (*Heliconoides inflatus*) from IODP Site U1461. **Table S2.** *Limacina* dissolution index and carbon and oxygen isotope data for pteropods (*Heliconoides inflatus*) and benthic foraminifera (*Uvigerina* spp.) from IODP Site U1463. **Table S3.** Calculated water temperatures and carbonate ion concentrations based on the $\delta^{13}C$ and $\delta^{18}O$ values of pteropods (*Heliconoides inflatus*) from IODP Site U1461. Water temperatures were calculated based on a linear regression devised for generic aragonitic marine organisms, which calcify in equilibrium with $\delta^{18}O_{sw}$ (Böhm et al, 2000). Carbonate ion concentrations are based on the species-specific correlation presented by Keul et al. (2017). **Table S4.** Calculated water temperatures and carbonate ion concentrations based on the $\delta^{13}C$ and $\delta^{18}O$ values of pteropods (*Heliconoides inflatus*) from IODP Site U1463. Water temperatures were calculated based on a linear regression devised for generic aragonitic marine organisms, which calcify in equilibrium with $\delta^{18}O_{sw}$ (Böhm et al, 2000). Carbonate ion concentrations are based on the species-specific correlation presented by Keul et al. (2017). **Fig. S1.** Seasonal profiles of water temperature (a.1–a.4), water temperature gradient (b.1–b.4), and salinity (c.1–c.4) at Site U1461 (gray; Station 273179) and Site U1463 (black; Station 278667). All temperature and salinity data were derived from the World Ocean Atlas 2018 (Locarnini et al. 2018). Also shown are profiles of the $\delta^{18}O$ values of seawater ($\delta^{18}O_{sw}$; d.1–d.4) derived from a regional calibration of the seawater salinity (Pei et al. 2021a, b).

Hallenberger *et al. Progress in Earth and Planetary Science*   (2022) 9:49

Page 13 of 15

Availability of data and materials
The datasets supporting the conclusions of this article are included within the article and its additional files.

Declarations

Competing interests
The authors declare that they have no competing interests.

Author details
[1] Energy and Mineral Resources Group (EMR), Geological Institute, RWTH Aachen University, Wuellnerstrasse 2, 52062 Aachen, Germany. [2] Institute of Geosciences, CAU Kiel, Ludewig-Meyn-Strasse 10, 24118 Kiel, Germany. [3] Institute of Geology and Paleontology, Graduate School of Science, Tohoku University, Aramaki-aza-aoba 6-3, Aoba-ku, Sendai 980-8578, Japan. [4] National Institute of Polar Research, Midori-cho 10-3, Tachikawa-shi, Tokyo 190-8518, Japan. [5] Atmosphere and Ocean Research Institute, The University of Tokyo, Kashiwanoha 5-1-5, Kashiwa-shi, Chiba 277-8564, Japan.

References
Almogi-Labin A, Hemleben C, Deuser W (1988) Seasonal variation in the flux of euthecosomatous pteropods collected in a deep sediment trap in the Sargasso Sea. Deep Sea Res Part A Oceanogr Res Pap 35(3):441–464

Almogi-Labin A, Hemleben C, Meischner D, Erlenkeuser H (1991) Paleoenvironmental events during the last 13,000 years in the central Red Sea as recorded by pteropoda. Paleoceanography 6(1):83–98

Bé A, Gilmer R (1977) A zoogeographic and taxonomic review of euthecosomatous Pteropoda. Ocean Micropaleontol 1(6):733–808

Bednaršek N, Možina J, Vogt M, O'Brien C, Tarling GA (2012) The global distribution of pteropods and their contribution to carbonate and carbon biomass in the modern ocean. Earth Syst Sci Data 4(1):167–186

Böhm F, Joachimski MM, Dullo W-C, Eisenhauer A, Lehnert H, Reitner J, Wörheide G (2000) Oxygen isotope fractionation in marine aragonite of coralline sponges. Geochim Cosmochim Acta 64(10):1695–1703

Bowman GM (1985) Oceanic reservoir correction for marine radiocarbon dates from northwestern Australia. Aust Archaeol 20:58–67

Broecker W, McGee D (2013) The 13C record for atmospheric CO2: what is it trying to tell us? Earth Planet Sci Lett 368:175–182

Chen C, Bé AW (1964) Seasonal distributions of euthecosomatous pteropods in the surface waters of five stations in the western North Atlantic. Bull Mar Sci 14(2):185–220

Condie S, Fandry C, McDonald D, Parslow J, Sainsbury K (2003) Linking ocean models to coastal management on Australia's North West Shelf. EOS Trans Am Geophys Union 84(6):49–53

Courtillat M, Hallenberger M, Bassetti M-A, Aubert D, Jeandel C, Reuning L, Korpanty C, Moissette P, Mounic S, Saavedra-Pellitero M (2020) New record of dust input and provenance during glacial periods in Western Australia Shelf (IODP expedition 356, Site U1461) from the Middle to Late Pleistocene. Atmosphere 11(11):1251

Curry WB, Duplessy J-C, Labeyrie L, Shackleton NJ (1988) Changes in the distribution of δ13C of deep water ΣCO2 between the last glaciation and the Holocene. Paleoceanography 3(3):317–341

d'Orbigny AD (1843) Voyage dans l'Amérique méridionale (le Brésil, la république orientale de l'Uruguay, la république Argentine, la Patagonie, la république du Chili, la republ. de Bolivia, la républ. du Pérou), exécuté pendant les années 1826, 1827, 1828, 1829, 1830, 1831, 1832 et 1833. Pitois-Levrault, Strasbourg

D'Adamo N, Fandry C, Buchan S, Domingues C (2009) Northern sources of the Leeuwin current and the "Holloway Current" on the North West Shelf. J R Soc West Aust 92:53–66

De Deckker P, Barrows TT, Rogers J (2014) Land–sea correlations in the Australian region: post-glacial onset of the monsoon in northwestern Western Australia. Quatern Sci Rev 105:181–194

Dix GR, James NP, Kyser TK, Bone Y, Collins LB (2005) Genesis and dispersal of carbonate mud relative to late quaternary sea-level change alogn a distally-steepened carbonate ramp (Northwester Shelf, Western Australia). J Sediment Res 75:665–678

Duplessy J, Shackleton N, Fairbanks R, Labeyrie L, Oppo D, Kallel N (1988) Deepwater source variations during the last climatic cycle and their impact on the global deepwater circulation. Paleoceanography 3(3):343–360

Fabry V, Deuser W (1992) Seasonal changes in the isotopic compositions and sinking fluxes of euthecosomatous pteropod shells in the Sargasso Sea. Paleoceanography 7(2):195–213

Fandry C, Steedman R (1994) Modelling the dynamics of the transient, barotropic response of continental shelf waters to tropical cyclones. Cont Shelf Res 14(15):1723–1750

Feng M, Li Y, Meyers G (2004) Multidecadal variations of Fremantle sea level: Footprint of climate variability in the tropical Pacific. Geophysical Research Letters 31(16):L16302

Feng M, McPhaden MJ, Xie S-P, Hafner J (2013) La Niña forces unprecedented Leeuwin Current warming in 2011. Sci Rep 3(1):1–9

Fontanier C, Jorissen F, Chaillou G, David C, Anschutz P, Lafon V (2003) Seasonal and interannual variability of benthic foraminiferal faunas at 550 m depth in the Bay of Biscay. Deep Sea Res Part I 50(4):457–494

Gallagher S, Reuning L, Himmler T, Henderiks J, De Vleeschouwer D, Groeneveld J, Lari AR, Fulthorpe C, Bogus K, Renema W (2018) The enigma of rare Quaternary oolites in the Indian and Pacific Oceans: A result of global oceanographic physicochemical conditions or a sampling bias? Quatern Sci Rev 200:114–122

Gallagher SJ, Fullthorpe CS, Bogus H, Scientists tE (2017a) Site U1461. Proceedings of the international ocean discovery program

Gallagher SJ, Fullthorpe CS, Bogus H, Scientists tE (2017b) Site U1463. In: Proceedings of the international ocean discovery program, 356

Gallagher SJ, Wallace MW, Hoiles PW, Southwood JM (2014) Seismic and stratigraphic evidence for reef expansion and onset of aridity on the Northwest Shelf of Australia during the Pleistocene. Mar Pet Geol 57:470–481

Gerhardt S, Groth H, Rühlemann C, Henrich R (2000) Aragonite preservation in late Quaternary sediment cores on the Brazilian Continental Slope: implications for intermediate water circulation. Int J Earth Sci 88(4):607–618

Gerhardt S, Henrich R (2001) Shell preservation of Limacina inflata (Pteropoda) in surface sediments from the Central and South Atlantic Ocean: a new proxy to determine the aragonite saturation state of water masses. Deep Sea Res Part I 48(9):2051–2071

Grossman EL, Betzer PR, Dudley WC, Dunbar RB (1986) Stable isotopic variation in pteropods and atlantids from North Pacific sediment traps. Mar Micropaleontol 10(1–3):9–22

Grossman EL, Ku T-L (1986) Oxygen and carbon isotope fractionation in biogenic aragonite: temperature effects. Chem Geol Isotope Geosci Sect 59:59–74

Hallegraeff G, Jeffrey S (1984) Tropical phytoplankton species and pigments of continental shelf waters of north and north-west Australia. Mar Ecol Prog Ser Oldendorf 20(1):59–74

Hallenberger M, Reuning L, Back S, Gallagher SJ, Iwatani H, Lindhorst K (2021) Climate and sea-level controlling internal architecture of a Quaternary carbonate ramp (Northwest Shelf of Australia). Sedimentology. https://doi.org/10.1111/sed.12948

Hallenberger M, Reuning L, Gallagher SJ, Back S, Ishiwa T, Christensen BA, Bogus K (2019) Increased fluvial runoff terminated inorganic aragonite precipitation on the Northwest Shelf of Australia during the early Holocene. Sci Rep 9(1):1–9

Harris P, Diaz MR, Eberli GP (2019) The formation and distribution of modern ooids on Great Bahama Bank. Ann Rev Mar Sci 11:491–516

Haslett J, Parnell A (2008) A simple monotone process with application to radiocarbon-dated depth chronologies. J R Stat Soc Ser C (Appl Stat) 57(4):399–418

Heaton TJ, Köhler P, Butzin M, Bard E, Reimer RW, Austin WE, Ramsey CB, Grootes PM, Hughen KA, Kromer B (2020) Marine20—the marine radiocarbon age calibration curve (0–55,000 cal BP). Radiocarbon 62(4):779–820

Hallenberger *et al. Progress in Earth and Planetary Science*   (2022) 9:49

Page 14 of 15

Hesse PP, Magee JW, van der Kaars S (2004) Late Quaternary climates of the Australian arid zone: a review. Quatern Int 118:87–102

Humphreys M, Pierrot D, van Heuven S (2020) PyCO2SYS: marine carbonate system calculations in Python. Version 1.3. 0. Zenodo. https://doi.org/10.5281/zenodo.3744275

Ishiwa T, Yokoyama Y, Reuning L, McHugh CM, De Vleeschouwer D, Gallagher SJ (2019) Australian Summer Monsoon variability in the past 14,000 years revealed by IODP Expedition 356 sediments. Prog Earth Planet Sci 6(1):17

James NP, Bone Y, Kyser TK, Dix GR, Collins LB (2004) The importance of changing oceanography in controlling late Quaternary carbonate sedimentation on a high-energy, tropical, oceanic ramp: north-western Australia. Sedimentology 51(6):1179–1205

Janssen AW (2012) Early Pliocene heteropods and pteropods (Mollusca, Gastropoda) from Le Puget-sur-Argens (Var). France Cainozoic Res 9(2):145–166

Jasper JP, Deuser WG (1993) Annual cycles of mass flux and isotopic composition of pteropod shells settling into the deep Sargasso Sea. Deep Sea Res Part I 40(4):653–669

Jonkers L, Kučera M (2015) Global analysis of seasonality in the shell flux of extant planktonic Foraminifera. Biogeosciences 12(7):2207–2226

Juranek L, Russell A, Spero H (2003) Seasonal oxygen and carbon isotope variability in euthecosomatous pteropods from the Sargasso Sea. Deep Sea Res Part I 50(2):231–245

Keul N, Langer G, de Nooijer LJ, Nehrke G, Reichart GJ, Bijma J (2013) Incorporation of uranium in benthic foraminiferal calcite reflects seawater carbonate ion concentration. Geochem Geophys Geosyst 14(1):102–111

Keul N, Peijnenburg K, Andersen N, Kitidis V, Goetze E, Schneider R (2017) Pteropods are excellent recorders of surface temperature and carbonate ion concentration. Sci Rep 7(1):12645

Key RM, Kozyr A, Sabine CL, Lee K, Wanninkhof R, Bullister JL, Feely RA, Millero FJ, Mordy C, Peng TH (2004) A global ocean carbon climatology: results from Global Data Analysis Project (GLODAP). Global Biogeochem Cycles. https://doi.org/10.1029/2004GB002247

Klöcker R, Ganssen G, Jung SJ, Kroon D, Henrich R (2006) Late Quaternary millennial-scale variability in pelagic aragonite preservation off Somalia. Mar Micropaleontol 59(3–4):171–183

Kuhnt W, Holbourn A, Xu J, Opdyke B, De Deckker P, Röhl U, Mudelsee M (2015) Southern Hemisphere control on Australian monsoon variability during the late deglaciation and Holocene. Nat Commun 6:5916

Lambeck K, Rouby H, Purcell A, Sun Y, Sambridge M (2014) Sea level and global ice volumes from the Last Glacial Maximum to the Holocene. Proc Natl Acad Sci 111(43):15296–15303

Lazar B, Erez J (1992) Carbon geochemistry of marine-derived brines: I 13C depletions due to intense photosynthesis. Geochimica et Cosmochimica Acta 56(1):335–345

Li F, Yan J, Chen Z-Q, Ogg JG, Tian L, Korngreen D, Liu K, Ma Z, Woods AD (2015) Global oolite deposits across the Permian-Triassic boundary: a synthesis and implications for palaeoceanography immediately after the end-Permian biocrisis. Earth Sci Rev 149:163–180

Locarnini M, Mishonov A, Baranova O et al (2018) World ocean atlas 2018, volume 1: Temperature (2018)https://archimer.ifremer.fr/doc/00651/76338/. Accessed 01.11.2021

Lough J (1998) Coastal climate of northwest Australia and comparisons with the Great Barrier Reef: 1960 to 1992. Coral Reefs 17(4):351–367

Mahjabin T, Pattiaratchi C, Hetzel Y (2020) Occurrence and seasonal variability of Dense Shelf Water Cascades along Australian continental shelves. Sci Rep 10(1):1–13

Manno C, Bednaršek N, Tarling GA, Peck VL, Comeau S, Adhikari D, Bakker DC, Bauerfeind E, Bergan AJ, Berning MI (2017) Shelled pteropods in peril: assessing vulnerability in a high CO2 world. Earth Sci Rev 169:132–145

Marchitto T, Curry W, Lynch-Stieglitz J, Bryan S, Cobb K, Lund D (2014) Improved oxygen isotope temperature calibrations for cosmopolitan benthic foraminifera. Geochim Cosmochim Acta 130:1–11

Martínez JI, Dedeckker P, Barrows TT (1999) Palaeoceanography of the last glacial maximum in the eastern Indian Ocean: planktonic foraminiferal evidence. Palaeogeogr Palaeoclimatol Palaeoecol 147(1–2):73–99

McGee D, Marcantonio F, Lynch-Stieglitz J (2007) Deglacial changes in dust flux in the eastern equatorial Pacific. Earth Planet Sci Lett 257(1–2):215–230

Monnin E, Indermühle A, Dällenbach A, Flückiger J, Stauffer B, Stocker TF, Raynaud D, Barnola J-M (2001) Atmospheric CO2 concentrations over the last glacial termination. Science 291(5501):112–114

Moyer R, Grottoli A (2011) Coral skeletal carbon isotopes (δ13C and Δ14C) record the delivery of terrestrial carbon to the coastal waters of Puerto Rico. Coral Reefs 30(3):791–802

Murgese DS, De Deckker P (2007) The Late Quaternary evolution of water masses in the eastern Indian Ocean between Australia and Indonesia, based on benthic foraminifera faunal and carbon isotopes analyses. Palaeogeogr Palaeoclimatol Palaeoecol 247(3–4):382–401

Nakayama H, Iijima H, Nakamura N, Kayanne H (2008) Carbon and oxygen stable isotope ratios of GSJ carbonate reference materials (JCp-1 and JCt-1). Bull Geol Surv Jp 59:461–466

Niebler H-S, Hubberten H-W, Gersonde R (1999) Oxygen isotope values of planktic foraminifera: a tool for the reconstruction of surface water stratification. In: Fischer G, Wefer G (eds) Use of proxies in paleoceanography. Springer, Berlin, pp 165–189

O'Connor S, Ulm S, Fallon SJ, Barham A, Loch I (2010) Pre-bomb marine reservoir variability in the Kimberley region. Western Australia Radiocarbon 52(3):1158–1165

Oakes RL, Davis CV, Sessa JA (2021) Using the stable isotopic composition of *Heliconoides inflatus* pteropod shells to determine calcification depth in the Cariaco Basin. Front Mar Sci 7:1169

Oakes RL, Sessa JA (2020) Determining how biotic and abiotic variables affect the shell condition and parameters of Heliconoides inflatus pteropods from a sediment trap in the Cariaco Basin. Biogeosciences 17(7):1975–1990

Ohga T, Kitazato H (1997) Seasonal changes in bathyal foraminiferal populations in response to the flux of organic matter (Sagami Bay, Japan). Terra Nova 9(1):33–37

Okai T, Suzuki A, Shigeru T, Inoue M, Nohara M, Kawahata H, Imai N (2004) Collaborative analysis of GSJ/AIST geochemical reference materials JCp-1 (Coral) and JCt-1 (Giant Clam). Chikyukagaku (Geochemistry) 38(4):281–286

Orr JC, Fabry VJ, Aumont O, Bopp L, Doney SC, Feely RA, Gnanadesikan A, Gruber N, Ishida A, Joos F (2005) Anthropogenic ocean acidification over the twenty-first century and its impact on calcifying organisms. Nature 437(7059):681–686

Pattiaratchi C (2006) Surface and sub-surface circulation and water masses off Western Australia. Bull Aust Meteorol Oceanogr Soc 19(5):95–104

Pei R, Kuhnt W, Holbourn A, Hingst J, Koppe M, Schultz J, Kopetz P, Zhang P, Andersen N (2021a) Monitoring Australian Monsoon variability over the past four glacial cycles. Palaeogeogr Palaeoclimatol Palaeoecol. https://doi.org/10.1016/j.palaeo.2021.110280

Pei R, Kuhnt W, Holbourn A, Jöhnck J, Hingst J, Beil S, Lübbers J, Andersen N (2021b) Evolution of sea surface hydrology along the Western Australian margin over the past 450 kyr. Paleoceanography and Paleoclimatology. https://doi.org/10.1029/2021PA004222

Peterson CD, Lisiecki LE, Stern JV (2014) Deglacial whole-ocean δ13C change estimated from 480 benthic foraminiferal records. Paleoceanography 29(6):549–563

Purkis S, Cavalcante G, Rohtla L, Oehlert AM, Harris PM, Swart PK (2017) Hydrodynamic control of whitings on Great Bahama Bank. Geology 45(10):939–942

Rahimpour-Bonab H, Bone Y, Moussavi-Harami R (1997) Stable isotope aspects of modern molluscs, brachiopods, and marine cements from cool-water carbonates, Lacepede Shelf. South Australia Geochimica Et Cosmochimica Acta 61(1):207–218

Raitzsch M, Kuhnert H, Hathorne EC, Groeneveld J, Bickert T (2011) U/Ca in benthic foraminifers: a proxy for the deep-sea carbonate saturation. Geochem Geophys Geosyst 12(6):Q06019

Ramsey CB (2009) Bayesian analysis of radiocarbon dates. Radiocarbon 51(1):337–360

Ravelo A, Fairbanks R (1992) Oxygen isotopic composition of multiple species of planktonic foraminifera: Recorders of the modern photic zone temperature gradient. Paleoceanography 7(6):815–831

Reimer PJ, Reimer RW (2001) A marine reservoir correction database and on-line interface. Radiocarbon 43(2A):461–463

Reuning L, Deik H, Petrick B, Auer G, Takayanagi H, Iryu Y, Courtillat M, Bassetti M-A (2022) Contrasting intensity of aragonite dissolution

and dolomite cementation in glacial versus interglacial intervals of a subtropical carbonate succession. Sedimentology.69(5):2131–2150

Robbins L, Blackwelder P (1992) Biochemical and ultrastructural evidence for the origin of whitings: a biologically induced calcium carbonate precipitation mechanism. Geology 20(5):464–468

Rochford DJ (1988) Seasonal influx of nitrates to the slope and shelf waters off north-west Australia. Commonwealth Scientific and Industrial Research Organisation, Marine Research Laboratories, Melbourne

Roger LM, Richardson AJ, McKinnon AD, Knott B, Matear R, Scadding C (2012) Comparison of the shell structure of two tropical Thecosomata (*Creseis acicula* and *Diacavolinia longirostris*) from 1963 to 2009: potential implications of declining aragonite saturation. ICES J Mar Sci 69(3):465–474

Sarnthein M, Grootes P, Holbourn A, Kuhnt W, Kühn H (2011) Tropical warming in the Timor Sea led deglacial Antarctic warming and atmospheric CO2 rise by more than 500 yr. Earth Planet Sci Lett 302(3–4):337–348

Sautter LR, Thunell RC (1991) Seasonal variability in the δ18O and δ13C of planktonic foraminifera from an upwelling environment: sediment trap results from the San Pedro Basin. Southern California Bight Paleoceanography 6(3):307–334

Scourse J, Kennedy H, Scott G, Austin W (2004) Stable isotopic analyses of modern benthic foraminifera from seasonally stratified shelf seas: disequilibria and the "seasonal effect." The Holocene 14(5):747–758

Shackleton NJ, Opdyke ND (1973) Oxygen isotope and palaeomagnetic stratigraphy of Equatorial Pacific core V28–238: Oxygen isotope temperatures and ice volumes on a 105 year and 106 year scale. Quatern Res 3(1):39–55

Sharma T, Clayton RN (1965) Measurement of O18O16 ratios of total oxygen of carbonates. Geochim Cosmochim Acta 29(12):1347–1353

Shinn EA, Steinen RP, Lidz BH, Swart PK (1989) Whitings, a sedimentologic dilemma. J Sediment Res 59(1):147–161

Spero HJ, Mielke KM, Kalve EM, Lea DW, Pak DK (2003) Multispecies approach to reconstructing eastern equatorial Pacific thermocline hydrography during the past 360 kyr. Paleoceanography. https://doi.org/10.1029/2002PA000814

Spooner MI, De Deckker P, Barrows TT, Fifield LK (2011) The behaviour of the Leeuwin Current offshore NW Australia during the last five glacial–interglacial cycles. Global Planet Change 75(3–4):119–132

Sreevidya E, Sijinkumar A, Nath BN (2019) Aragonite pteropod abundance and preservation records from the Maldives, equatorial Indian Ocean: inferences on past oceanic carbonate saturation and dissolution events. Palaeogeogr Palaeoclimatol Palaeoecol 534:109313. https://doi.org/10.1016/j.palaeo.2019.109313

Sudmeyer R (2016) Climate in the Pilbara

Tarutani T, Clayton RN, Mayeda TK (1969) The effect of polymorphism and magnesium substitution on oxygen isotope fractionation between calcium carbonate and water. Geochim Cosmochim Acta 33(8):987–996

R: A language and environment for statistical computing (2018) R. C. Team. https://www.R-project.org/. Accessed 01.11.2021

Tozuka T, Kataoka T, Yamagata T (2014) Locally and remotely forced atmospheric circulation anomalies of Ningaloo Niño/Niña. Clim Dyn 43(7):2197–2205

Trower EJ, Lamb MP, Fischer WW (2017) Experimental evidence that ooid size reflects a dynamic equilibrium between rapid precipitation and abrasion rates. Earth Planet Sci Lett 468:112–118

Utami DA, Reuning L, Hallenberger M, Cahyarini SY (2021) The mineralogic and isotopic fingerprint of equatorial carbonates: Kepulauan Seribu, Indonesia. Int J Earth Sci 110(2):513–534

Van der Kaars S, De Deckker P, Gingele FX (2006) A 100 000-year record of annual and seasonal rainfall and temperature for northwestern Australia based on a pollen record obtained offshore. J Quat Sci 21(8):879–889

Venancio IM, Belem AL, Santos TP, Lessa DO, Albuquerque ALS, Mulitza S, Schulz M, Kucera M (2017) Calcification depths of planktonic foraminifera from the southwestern Atlantic derived from oxygen isotope analyses of sediment trap material. Mar Micropaleontol 136:37–50

Wall-Palmer D, Metcalfe B, Leng MJ, Sloane HJ, Ganssen G, Vinayachandran P, Smart CW (2018) Vertical distribution and diurnal migration of atlantid heteropods. Mar Ecol Prog Ser 587:1–15

Wall-Palmer D, Smart CW, Hart MB (2013) In-life pteropod shell dissolution as an indicator of past ocean carbonate saturation. Quatern Sci Rev 81:29–34

Wall-Palmer D, Smart CW, Hart MB, Leng MJ, Borghini M, Manini E, Aliani S, Conversi A (2014) Late Pleistocene pteropods, heteropods and planktonic foraminifera from the Caribbean Sea, Mediterranean Sea and Indian Ocean. Micropaleontology 60:557–578

Wejnert KE, Pride CJ, Thunell RC (2010) The oxygen isotope composition of planktonic foraminifera from the Guaymas Basin, Gulf of California: Seasonal, annual, and interspecies variability. Mar Micropaleontol 74(1–2):29–37

Wormuth JH (1981) Vertical distributions and diel migrations of Euthecosomata in the northwest Sargasso Sea. Deep Sea Res Part A Oceanogr Res Pap 28(12):1493–1515

Xu J, Holbourn A, Kuhnt W, Jian Z, Kawamura H (2008) Changes in the thermocline structure of the Indonesian outflow during Terminations I and II. Earth Planet Sci Lett 273(1–2):152–162

Yokoyama Y, Miyairi Y, Aze T, Yamane M, Sawada C, Ando Y, de Natris M, Hirabayashi S, Ishiwa T, Sato N (2019) A single stage accelerator mass spectrometry at the Atmosphere and Ocean Research Institute, The University of Tokyo. Nucl Instrum Methods Phys Res, Sect B 455:311–316

Yu J, Elderfield H (2007) Benthic foraminiferal B/Ca ratios reflect deep water carbonate saturation state. Earth Planet Sci Lett 258(1–2):73–86

Yu J, Foster GL, Elderfield H, Broecker WS, Clark E (2010) An evaluation of benthic foraminiferal B/Ca and δ11B for deep ocean carbonate ion and pH reconstructions. Earth Planet Sci Lett 293(1–2):114–120

Zeebe RE, Wolf-Gladrow D (2001) CO2 in seawater: equilibrium, kinetics, isotopes. Elsevier, Amsterdam

Zinke J, Hoell A, Lough J, Feng M, Kuret A, Clarke H, Ricca V, Rankenburg K, McCulloch M (2015) Coral record of southeast Indian Ocean marine heatwaves with intensified Western Pacific temperature gradient. Nat Commun 6(1):1–9

Zweng M, Seidov D, Boyer T, Locarnini M, Garcia H, Mishonov A, Baranova O, Weathers K, Paver C, Smolyar I (2019). World ocean atlas 2018, volume 2: Salinity.

Publisher's Note